



**HAL**  
open science

# A combined Finite Volumes -Finite Elements method for a low-Mach model: Application to the simulation of a transient injection flow

Caterina Calgaro, Claire Colin, Emmanuel Creusé

## ► To cite this version:

Caterina Calgaro, Claire Colin, Emmanuel Creusé. A combined Finite Volumes -Finite Elements method for a low-Mach model: Application to the simulation of a transient injection flow. 2017. hal-01574894v1

**HAL Id: hal-01574894**

**<https://hal.science/hal-01574894v1>**

Preprint submitted on 16 Aug 2017 (v1), last revised 14 Dec 2018 (v2)

**HAL** is a multi-disciplinary open access archive for the deposit and dissemination of scientific research documents, whether they are published or not. The documents may come from teaching and research institutions in France or abroad, or from public or private research centers.

L'archive ouverte pluridisciplinaire **HAL**, est destinée au dépôt et à la diffusion de documents scientifiques de niveau recherche, publiés ou non, émanant des établissements d'enseignement et de recherche français ou étrangers, des laboratoires publics ou privés.

# A combined Finite Volumes - Finite Elements method for a low-Mach model: Application to the simulation of a transient injection flow.

Caterina Calgaro\*, Claire Colin<sup>†</sup> and Emmanuel Creusé<sup>‡</sup>

August 16, 2017

Univ. Lille, CNRS, UMR 8524 - Laboratoire Paul Painlevé, F-59000  
Lille, France.

*and*

INRIA Lille Nord Europe, EPI RAPSODI  
Parc scientifique de la Haute Borne  
40, avenue Halley - Bât A - Park Plaza  
59650 Villeneuve d'Ascq, France.

## Abstract

In this paper, we develop a combined Finite Volumes - Finite Elements method based on a time splitting to simulate some low-Mach flows. The mass conservation equation is solved by a Vertex-Based Finite Volume scheme using a  $\tau$ -limiter. The momentum equation associated with the compressibility constraint is solved by a Finite Element projection scheme. The originality of the approach is twofold. First, the state equation linking the temperature, the density and the thermodynamic pressure is imposed implicitly. Second, the proposed combined scheme preserves the constant states, in the same way as a similar one previously developed for the variable density Navier-Stokes system. Some numerical tests are performed to exhibit the efficiency on the scheme. On one hand, academic tests illustrate the ability of the scheme in term of convergence rates in time and space. On the other hand, our results are compared to some of the literature by simulating a transient injection flow.

**Key Words:** Low-Mach model, Finite Volume method, Finite Element method, Projection scheme.

---

\*caterina.calgaro@univ-lille.fr

<sup>†</sup>claire.lecerf@ed.univ-lille1.fr

<sup>‡</sup>emmanuel.creuse@univ-lille.fr

# 1 Introduction

Variable density - low Mach numbers flows have been widely studied in the recent literature because of their applicability in various phenomena such as flows in high-temperature gas reactors, meteorological flows, flows with convective and/or conductive heat transfert, combustion processes and many others. In such cases, the resolution of the full compressible Navier-Stokes system is not adapted, because of the sound waves speed which move much faster than the entropy or the vorticity ones. Consequently, this choice would impose a too strong time-step limitation in the framework of explicit solvers, leading to unreachable numerical simulations. The Boussinesq incompressible model is not a better alternative for such low-speed phenomena. Indeed, the compressibility effects can not be totally canceled because of large variations of temperature and density, even if pressure ones are much smaller. Consequently, some models have been formally derived, leading to the filtering of the acoustic waves by the use of some formal asymptotic expansions [24, 21, 30].

Like mentioned in [2], there exists two families of methods to compute flows at low-Mach number regime. On one hand, there are the so-called density-based solvers, corresponding to methods used for the simulation of supersonic and transonic flows, which have been adapted to make them efficient and robust in the case of a low-Mach flow [18, 28], using for example some preconditionning techniques [32, 23]. On the other hand, there are the so-called pressure-based solvers, coming from the incompressible case. The pressure variations become independent from the state equation, and are coupled to the divergence condition on the velocity [26]. In that case, a fractional step method initially developed in [6, 7, 31] and progressively improved in [13, 14, 12, 15, 16] is used most of the time. The pressure field comes from the resolution of a Poisson equation, for which the right-hand side contains some time derivative of the density term (see e.g. [2], Asymptotic approach 2). Concerning the space discretisation, lots of papers deal with Finite Element methods [19, 25], which can also be stabilized in the case of convection dominated regimes [29, 22, 10, 11, 1]. Others are also devoted to Finite Differences [27, 9, 20].

In this paper, we propose a combined Finite Volume - Finite Element method, which was initially developed for the simulation of incompressible and variable density flows [4]. This method is based on a time splitting allowing to solve the mass conservation equation by a Finite Volume method, and the momentum equation associated with the free divergence constraint on the velocity by a Finite Element one. It allows in particular to preserve the stationary states and to ensure the discrete maximum principle on the density [3]. It also has been used to simulate some mixture flows such as avalanches [5]. Following the same philosophy, we propose to adapt this method to the case of a low-Mach model, providing a new pressure-based solver. The originality of our approach lies in the fact that the density is computed from the mass equation with a Finite Volume method, the other variables of the problem being approximated by a

Finite Element method. In our work, the equation of state is not explicitly imposed. Moreover, the scheme recovers the properties of our previous proposed scheme at the incompressible limit [4, 3].

The paper is organized as follows. In Section 2 the governing equations are recalled, and the choice of the final system to be solved is justified among several equivalent sets of equations. In Section 3, the combined Finite Volumes - Finite Elements is carefully described. Section 4 is devoted to some numerical simulations to exhibit the ability of the code. First, some analytical benchmarks are proposed and underline the accuracy of the scheme. Then, a transient injection flow is simulated [2, 11, 1].

## 2 Governing equations

### 2.1 Choice of the system

The equations modelling low Mach number flows are derived by inserting the asymptotic expansions of the variables with respect to the Mach number  $M$  of the problem in the Navier-Stokes compressible equations [24, 2]. One of the characteristics of the process is that the pressure splits into two terms. Denoting  $\mathbf{x} \in \mathbb{R}^2$  the space variable and  $t \in \mathbb{R}_*^+$  the time one, we write:

$$p(\mathbf{x}, t) = P(t) + \pi(\mathbf{x}, t),$$

where  $P$  is called the thermodynamic pressure and  $\pi$  the dynamic pressure.  $P$  only depends on  $t$ , and  $\pi$  is in the order of  $M^2$ . According to single time scale and single space scale asymptotics, the continuity, momentum and temperature equations, as well as the equation of state for a calorifically perfect gas in adimensioned form in an open polygonal domain  $\Omega \subset \mathbb{R}^2$  are given by [2]:

$$\frac{\partial \rho}{\partial t} + \nabla \cdot (\rho \mathbf{u}) = 0, \quad (1)$$

$$\rho \left( \frac{\partial \mathbf{u}}{\partial t} + \mathbf{u} \cdot \nabla \mathbf{u} \right) + \frac{1}{\gamma} \nabla \pi - \frac{1}{\text{Re}} \nabla \cdot \boldsymbol{\tau} = -\frac{1}{\text{Fr}^2} \rho \mathbf{e}_y, \quad (2)$$

$$\rho \left( \frac{\partial T}{\partial t} + \mathbf{u} \cdot \nabla T \right) - \frac{1}{\gamma} \frac{dP}{dt} - \frac{1}{\text{Re Pr}} \Delta T = 0, \quad (3)$$

$$P = (\gamma - 1) \rho T, \quad (4)$$

where  $\rho$  is the density,  $\mathbf{u}$  the velocity and  $T$  the temperature. Here,  $\boldsymbol{\tau}$  is the viscosity stress tensor defined by

$$\boldsymbol{\tau} = \nabla \mathbf{u} + \nabla \mathbf{u}^T - \frac{2}{3} \nabla \cdot \mathbf{u} \mathbf{I},$$

and  $\mathbf{e}_y = (0, 1)^T$ . The adimensional characteristic numbers of the flow are given by:

- The gas specific heat ratio  $\gamma = 1.4$ ,
- The Reynolds number

$$\text{Re} = \frac{u_{ref} l_{ref}}{\nu},$$

with  $u_{ref}$  and  $l_{ref}$  some characteristic velocity and length and  $\nu$  the kinematic viscosity of the flow,

- The Prandtl number

$$\text{Pr} = \frac{\mu c_p}{\lambda} = \frac{\nu}{\alpha},$$

with  $\mu$  the dynamic viscosity,  $c_p$  the heat massic capacity,  $\lambda$  the heat conductivity and  $\alpha$  the heat diffusivity,

- The Froude number

$$\text{Fr} = \frac{u_{ref}}{\sqrt{g l_{ref}}},$$

with  $g$  the scalar-valued norm of the gravity field.

By combining (1), (3) and (4), we obtain:

$$\nabla \cdot \mathbf{u} = -\frac{1}{\gamma P} \frac{dP}{dt} + \frac{\gamma - 1}{\text{Re Pr } P} \Delta T. \quad (5)$$

In [2], two pressure-based schemes are proposed:

- In the first one, equations (2) and (3) are reformulated using (4), in order to make the density variable disappear, to obtain:

$$\frac{\partial \mathbf{u}}{\partial t} + \mathbf{u} \cdot \nabla \mathbf{u} = \frac{(\gamma - 1)T}{P} \left( -\frac{1}{\gamma} \nabla \pi + \frac{1}{\text{Re}} \nabla \cdot \boldsymbol{\tau} \right) - \frac{1}{\text{Fr}^2} \mathbf{e}_y, \quad (6)$$

$$\frac{\partial T}{\partial t} + \mathbf{u} \cdot \nabla T = \frac{(\gamma - 1)T}{P} \left( \frac{1}{\gamma} \frac{dP}{dt} + \frac{1}{\text{Re Pr}} \Delta T \right). \quad (7)$$

Equations (6) and (7) associated with the compressibility constraint (5) give a system in  $(T, \mathbf{u}, \pi, P)$ . The value of  $P$  is obtained either by an integration in space on the domain of equation (5) leading to the conservation of the internal energy over the total volume, or by an integration in space of equation (4) ensuring the mass conservation.

- In the second one, the density  $\rho$  is kept as an unknown, and the system to be solved is composed of (2)-(3)-(4) and (1), this last equation being used to express the compressibility constraint imposed to the velocity field. Like before, an equation has to be integrated in space to give the time evolution of  $P$ .

In this work, we propose a new way to proceed, using the fact that the system (1)-(2)-(3)-(4) is equivalent to the system (1)-(2)-(3) and (5). In particular, we easily verify that the equation of state (4) is implicitly imposed. Indeed, with the notation  $D_t = \frac{\partial}{\partial t} + \mathbf{u} \cdot \nabla$ , starting from (3) and using (5) to substitute the diffusive term, we get:

$$D_t T = \frac{1}{(\gamma - 1)\rho} \left( \frac{dP}{dt} + P \nabla \cdot \mathbf{u} \right). \quad (8)$$

Combining (8) with (1) gives:

$$D_t T = \frac{1}{(\gamma - 1)\rho} \frac{dP}{dt} - \frac{P}{(\gamma - 1)\rho^2} D_t \rho,$$

which is equivalent to:

$$D_t T = D_t \left( \frac{P}{(\gamma - 1)\rho} \right).$$

Consequently, supposing that the equation of state is initially fulfilled, we can deduce (4). The thermodynamic pressure time evolution is determined by integrating (5) over the domain  $\Omega$ :

$$\frac{dP}{dt} + \frac{\gamma P}{|\Omega|} \int_{\partial\Omega} \mathbf{u} \cdot \mathbf{n} = \frac{\gamma(\gamma - 1)}{|\Omega| \text{Re Pr}} \int_{\partial\Omega} \nabla T \cdot \mathbf{n}, \quad (9)$$

where  $\mathbf{n}$  is the outer unit normal to  $\Omega$  on  $\partial\Omega$ . In the following, we will consequently consider the system (1)-(2)-(3)-(5) and (9), where the unknowns are  $\rho$ ,  $T$ ,  $\mathbf{u}$ ,  $\pi$  and  $P$ .

## 2.2 Initial and boundary conditions

The initial conditions for the system (1)-(2)-(3)-(5) and (9) are given in  $\Omega$  by:

$$\mathbf{u}(\mathbf{x}, 0) = \mathbf{u}_0(\mathbf{x}), \quad T(\mathbf{x}, 0) = T_0(\mathbf{x}), \quad P(0) = P_0, \quad \rho(\mathbf{x}, 0) = \frac{P_0}{(\gamma - 1)T_0(\mathbf{x})}.$$

Concerning the boundary conditions, we set  $\overline{\partial\Omega} = \overline{\Gamma}_D \cup \overline{\Gamma}_N$  with  $\Gamma_D \cap \Gamma_N = \emptyset$ . We impose:

$$\begin{aligned} \mathbf{u} &= \mathbf{u}_D \quad \text{on } \partial\Omega, \\ T &= T_D \text{ and } \rho = \frac{P}{(\gamma - 1)T_D} \quad \text{on } \Gamma_D, \\ \nabla T \cdot \mathbf{n} &= \nabla \rho \cdot \mathbf{n} = 0 \quad \text{on } \Gamma_N. \end{aligned}$$

## 3 The combined Finite Volumes - Finite Elements method

The combined Finite Volumes - Finite Elements scheme (C-FV-FE scheme) is based on a time splitting, allowing in particular to solve equation (1) by a finite volumes solver,

and equations (2), (3), (5) by a finite elements one, using the same strategy as the one developed in [4] for the variable density incompressible Navier-Stokes system. We first describe the splitting used in time in order to reach the globally optimal accuracy in time according to the accuracy in time of each part of the scheme.

### 3.1 The time splitting

Let  $\Delta t$  be the time step and  $t^n = n\Delta t$ . We assume that  $P^{n-1}$ ,  $T^{n-1}$ ,  $\rho^{n-1}$ ,  $\mathbf{u}^{n-1}$  and  $\pi^{n-1}$  as well as  $P^n$ ,  $T^n$ ,  $\rho^n$ ,  $\mathbf{u}^n$  and  $\pi^n$  are known approximated values, respectively at times  $t^{n-1}$  and  $t^n$ .

1. The thermodynamic pressure  $P^{n+1}$  is computed by the resolution of the ordinary differential equation (9) using a BDF2-scheme in time and an extrapolation of the temperature:

$$\frac{3P^{n+1} - 4P^n + P^{n-1}}{2\Delta t} + \frac{\gamma P^{n+1}}{|\Omega|} \int_{\partial\Omega} \mathbf{u}_D^{n+1} \cdot \mathbf{n} = \frac{\gamma(\gamma - 1)}{|\Omega| \text{Re Pr}} \int_{\Gamma_D} \nabla(2T^n - T^{n-1}) \cdot \mathbf{n}. \quad (10)$$

2. The density  $\rho^{n+1}$  at time  $t^{n+1}$  is computed by solving the continuity equation (1) using a second order Runge-Kutta scheme in time:

$$\frac{\rho^{n+\frac{1}{2}} - \rho^n}{\Delta t} + \nabla \cdot (\rho^n \mathbf{u}^{n+\frac{1}{2}}) = 0, \quad (11)$$

$$\frac{\rho^{n+1} - \rho^n}{\Delta t} + \frac{1}{2} \left( \nabla \cdot (\rho^n \mathbf{u}^{n+\frac{1}{2}}) + \nabla \cdot (\rho^{n+\frac{1}{2}} \mathbf{u}^{n+\frac{1}{2}}) \right) = 0, \quad (12)$$

with

$$\mathbf{u}^{n+\frac{1}{2}} = \frac{(2\mathbf{u}^n - \mathbf{u}^{n-1}) + \mathbf{u}^n}{2} = \frac{3\mathbf{u}^n - \mathbf{u}^{n-1}}{2} \quad (13)$$

and:

$$\begin{aligned} \nabla \rho^{n+\frac{1}{2}} \cdot \mathbf{n} &= \nabla \rho^{n+1} \cdot \mathbf{n} = 0 \text{ on } \Gamma_N, \\ \rho^{n+1} &= \frac{P^{n+1}}{(\gamma - 1)T_D} \text{ on } \Gamma_D. \end{aligned}$$

3. The temperature  $T^{n+1}$  is computed by solving the temperature equation (3) using a BDF2-scheme in time and an extrapolation of the velocity:

$$\begin{aligned} \rho^{n+1} \left( \frac{3T^{n+1} - 4T^n + T^{n-1}}{2\Delta t} + (2\mathbf{u}^n - \mathbf{u}^{n-1}) \cdot \nabla T^{n+1} \right) \\ - \frac{1}{\gamma} \left( \frac{3P^{n+1} - 4P^n + P^{n-1}}{2\Delta t} \right) - \frac{1}{\text{Re Pr}} \Delta T^{n+1} = 0 \end{aligned} \quad (14)$$

and:

$$\begin{aligned} \nabla T^{n+1} \cdot \mathbf{n} &= 0 \text{ on } \Gamma_N, \\ T^{n+1} &= T_D \text{ on } \Gamma_D. \end{aligned}$$

4. The velocity  $\mathbf{u}^{n+1}$  and the pressure  $\pi^{n+1}$  are computed by solving the momentum equation (2) associated with the compressibility constraint (5) using a BDF2-scheme in time and an extrapolation of the velocity:

$$\rho^{n+1} \left( \frac{3\mathbf{u}^{n+1} - 4\mathbf{u}^n + \mathbf{u}^{n-1}}{2\Delta t} + (2\mathbf{u}^n - \mathbf{u}^{n-1}) \cdot \nabla \mathbf{u}^{n+1} \right) + \frac{1}{\gamma} \nabla \pi^{n+1} \quad (15)$$

$$\begin{aligned} -\frac{1}{\text{Re}} \nabla \cdot \boldsymbol{\tau}^{n+1} &= -\frac{1}{\text{Fr}^2} \rho^{n+1} \mathbf{e}_y, \\ \nabla \cdot \mathbf{u}^{n+1} &= -\frac{3P^{n+1} - 4P^n + P^{n-1}}{2\gamma\Delta t P^{n+1}} + \frac{\gamma - 1}{\text{Re Pr } P^{n+1}} \Delta T^{n+1}, \end{aligned} \quad (16)$$

with

$$\nabla \cdot \boldsymbol{\tau}^{n+1} = \Delta \mathbf{u}^{n+1} + \frac{1}{3} \nabla (\nabla \cdot (2\mathbf{u}^n - \mathbf{u}^{n-1})).$$

and

$$\mathbf{u}^{n+1} = \mathbf{u}_D \quad \text{on } \partial\Omega.$$

Note that in [4], the second order in time was obtained thanks to a Strang splitting. Indeed, the velocity used in the first step corresponding to the computation of the new density  $\rho^{n+1}$  was considered at time  $t^n$  and not extrapolated at time  $(t^n + t^{n+1})/2$  as indicated in (13), which is necessary to reach the second order accuracy. Note also that in [2], the proposed time splitting is basically at order one, and a fixed-point procedure is consequently added to increase the accuracy in time.

**Remark 3.1.** *As it will be explained in the next section, such a way to proceed allows in particular to solve the mass equation by a FV method. Consequently, it ensures a local mass conservation, while preserving the maximum principle on the density at the incompressible limit of the fluid. In that sense, the proposed numerical scheme can be seen as a generalization of the one previously developed for the variable density incompressible model [4]. Let us note moreover that in the case of another state equation than (4), the scheme can also be easily adapted by modifying equations (3) and (5).*

**Remark 3.2.** *Instead of solving the temperature equation (14), we could have in mind to use the state equation (4) to compute  $T^{n+1}$ . Nevertheless, this would lead to a lack of regularity of  $T^{n+1}$ , which is necessary in the constraint (16) in order to derive the values of  $\mathbf{u}^{n+1}$  and  $\pi^{n+1}$ .*

## 3.2 Space discretisation

The discretization in space is based on a triangulation of the domain  $\Omega$  by a set of triangles defining a regular mesh  $\tau_h$  in the Ciarlet sense [8]. Each component of the velocity  $\mathbf{u}_h$  is discretized by some  $\mathbb{P}_2$ -Lagrange finite elements, and the pressure  $\pi_h$  by some  $\mathbb{P}_1$ -Lagrange finite elements, leading to  $H^1(\Omega)$  conforming approximations fulfilling the usual discrete LBB condition and consequently ensuring the stability of

the discrete problem. The temperature  $T_h$  is also discretized by some  $\mathbb{P}_2$ -Lagrange finite elements, leading to a  $H^1(\Omega)$  conforming approximation. The density  $\rho_h$  is discretized by piecewise constant values on a dual mesh  $\tau_h^*$  associated with  $\tau_h$ , allowing to consider a vertex-based finite-volume schemes for the resolution of the mass equation. The density field can also be interpreted as a  $\mathbb{P}_1$ -Lagrange finite elements field, since a value of the density is naturally associated with each node of any triangles. The degrees of freedom of each variable corresponding to the space associated discretizations are displayed in Figure 1. For further details, we refer to [4].

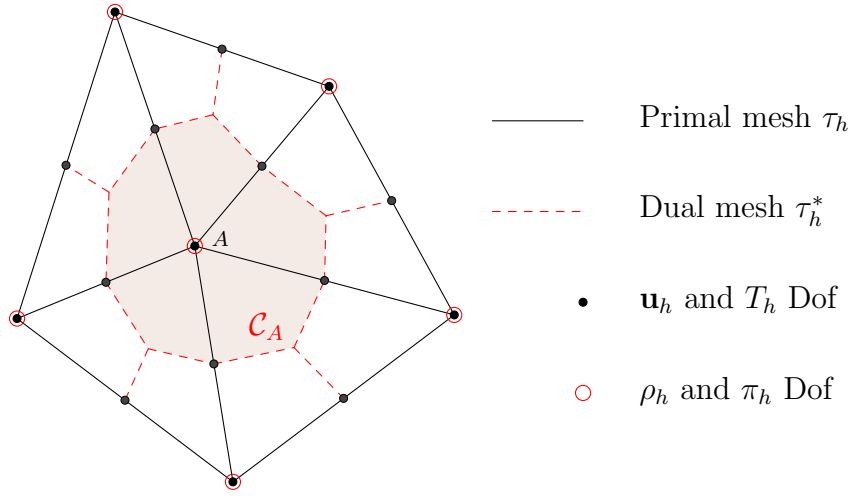


Figure 1: Space discretization: patch  $\Omega_A$ . Meshes and Degrees of Freedom (DoF) for each variable.

### 3.2.1 Solving the thermodynamic pressure

Assuming that the approximated values of  $P^n$ ,  $P^{n-1}$ ,  $T_h^n$  and  $T_h^{n-1}$  are known (step 1 of the time splitting), the value of  $P^{n+1}$  is simply computed by using the discrete version of equation (10), namely:

$$\frac{3P^{n+1} - 4P^n + P^{n-1}}{2\Delta t} + \frac{\gamma P^{n+1}}{|\Omega|} \int_{\partial\Omega} \mathbf{u}_D^{n+1} \cdot \mathbf{n} = \frac{\gamma(\gamma - 1)}{|\Omega| \text{Re Pr}} \int_{\Gamma_D} \nabla(2T_h^n - T_h^{n-1}) \cdot \mathbf{n}. \quad (17)$$

### 3.2.2 Solving the temperature by a FE method

Assuming that  $\rho_h^{n+1}$ ,  $T_h^n$ ,  $T_h^{n-1}$ ,  $\mathbf{u}_h^n$ ,  $\mathbf{u}_h^{n-1}$ ,  $P^{n+1}$ ,  $P^n$  and  $P^{n-1}$  are known (step 3 of the time splitting), the value of  $T_h^{n+1}$  is computed by the resolution the equation (14),

namely:

$$\begin{aligned} \rho_h^{n+1} \left( \frac{3T_h^{n+1} - 4T_h^n + T_h^{n-1}}{2\Delta t} + (2\mathbf{u}_h^n - \mathbf{u}_h^{n-1}) \cdot \nabla T_h^{n+1} \right) \\ - \frac{1}{\gamma} \left( \frac{3P^{n+1} - 4P^n + P^{n-1}}{2\Delta t} \right) - \frac{1}{\text{Re Pr}} \Delta T_h^{n+1} = 0. \end{aligned} \quad (18)$$

It is performed considering its weak finite elements formulation, associated with the boundary conditions specified in section 2.2.

### 3.2.3 Solving the velocity by a FE method

We detail here the projection method used to derive  $\mathbf{u}_h^{n+1}$  and  $\pi_h^{n+1}$  (step 4 of the time splitting), contrary to [4] in which an Uzawa solver was considered. It constitutes a natural adaptation from the section 4 of [15] to the low-Mach model case. We assume that  $\rho_h^{n+1}$ ,  $\pi_h^n$ ,  $P^{n+1}$ ,  $P^n$ ,  $P^{n-1}$  and  $T_h^{n+1}$  are known, as well as the auxiliary variables  $\tilde{\mathbf{u}}_h^n$ ,  $\tilde{\mathbf{u}}_h^{n-1}$ ,  $\phi_h^n$ , and  $\phi_h^{n-1}$  specific to the projection method (where  $(\tilde{\mathbf{u}}_h^0, \phi_h^0)$  and  $(\tilde{\mathbf{u}}_h^1, \phi_h^1)$  are initialized in the same way as in [15]). First, the velocity field  $\tilde{\mathbf{u}}_h^{n+1}$  which does not fulfill the constraint (5) is computed by solving the weak finite elements formulation of the parabolic equation:

$$\left\{ \begin{array}{l} \rho_h^{n+1} \left( \frac{3\tilde{\mathbf{u}}_h^{n+1} - 4\tilde{\mathbf{u}}_h^n + \tilde{\mathbf{u}}_h^{n-1}}{2\Delta t} + (2\tilde{\mathbf{u}}_h^n - \tilde{\mathbf{u}}_h^{n-1}) \cdot \nabla \tilde{\mathbf{u}}_h^{n+1} \right) \\ + \frac{1}{\gamma} \nabla \cdot \left( \pi_h^n + \frac{4}{3}\phi_h^n - \frac{1}{3}\phi_h^{n-1} \right) - \frac{1}{\text{Re}} \nabla \cdot \boldsymbol{\tau}_h^{n+1} = -\frac{1}{\text{Fr}^2} \rho_h^{n+1} \mathbf{e}_y, \\ \tilde{\mathbf{u}}_h^{n+1}|_{\partial\Omega} = \mathbf{u}_D^{n+1}, \end{array} \right.$$

associated with boundary conditions on the velocity given in section 2.2. Then, the pressure  $\pi_h^{n+1}$  is defined by :

$$\pi_h^{n+1} = \pi_h^n + \phi_h^{n+1}.$$

Here,  $\phi_h^{n+1}$  is the solution of the weak finite elements formulation of the elliptic equation given by:

$$\left\{ \begin{array}{l} \nabla \cdot \left( \frac{1}{\bar{\rho}_h^{n+1}} \nabla \phi_h^{n+1} \right) = \frac{3\gamma}{2\Delta t} \left( \nabla \cdot \tilde{\mathbf{u}}_h^{n+1} + \frac{3P^{n+1} - 4P^n + P^{n-1}}{2\gamma\Delta t P^{n+1}} \right. \\ \left. - \frac{(\gamma-1)}{\text{Re Pr } P^{n+1}} \Delta T_h^{n+1} \right), \\ \nabla \phi_h^{n+1} \cdot \mathbf{n}|_{\partial\Omega} = 0, \end{array} \right. \quad (19)$$

where for any triangle  $K \in \tau_h$  we define:

$$\frac{1}{\bar{\rho}_h^{n+1}|_K} = \frac{1}{3} \sum_{A_i \in K} \frac{1}{\rho_h^{n+1}(A_i)},$$

with  $A_i$  the three vertices belonging to the triangle  $K$ .

Finally  $\mathbf{u}_h^{n+1}$  is defined by:

$$\mathbf{u}_h^{n+1} = \tilde{\mathbf{u}}_h^{n+1} - \frac{2 \Delta t}{3 \gamma \bar{\rho}_h^{n+1}} \nabla \phi_h^{n+1}. \quad (20)$$

**Remark 3.3.** *From the discrete point of view,  $\tilde{\mathbf{u}}_h^{n+1}$  and  $\phi_h^{n+1}$  are computed by some finite element solver based on the usual variational formulations. Consequently, these two fields both belong to  $H^1(\Omega)$ . As we can see, it is not the case for  $\mathbf{u}_h^{n+1}$ , and the evaluation of its divergence can only be understood in a weak sense.*

### 3.2.4 Solving the density with a FV method

Assuming that  $\rho_h^n$ ,  $\mathbf{u}_h^n$  and  $\mathbf{u}_h^{n-1}$  are known (step 2 of the time splitting), the value of  $\rho_h^{n+1}$  is computed by the resolution of the discrete version of equations (11)-(12), namely:

$$\begin{aligned} \frac{\rho_h^{n+\frac{1}{2}} - \rho_h^n}{\Delta t} + \nabla \cdot (\rho_h^n \mathbf{u}_h^{n+\frac{1}{2}}) &= 0, \\ \frac{\rho_h^{n+1} - \rho_h^n}{\Delta t} + \frac{1}{2} \left( \nabla \cdot (\rho_h^n \mathbf{u}_h^{n+\frac{1}{2}}) + \nabla \cdot (\rho_h^{n+\frac{1}{2}} \mathbf{u}_h^{n+\frac{1}{2}}) \right) &= 0, \end{aligned}$$

with

$$\mathbf{u}_h^{n+\frac{1}{2}} = \frac{(2\mathbf{u}_h^n - \mathbf{u}_h^{n-1}) + \mathbf{u}_h^n}{2} = \frac{3\mathbf{u}_h^n - \mathbf{u}_h^{n-1}}{2}.$$

The Finite-Volume method is carefully detailed in [4], and its generalization to ensure the  $L^\infty$ -stability in the case of incompressible flows with the use of the so-called  $\tau$ -limiters is given in [3]. Here, we point out the fact that from values of  $\mathbf{u}_h^{n+\frac{1}{2}}$  obtained by the Finite Element scheme, we need to deduce values of  $\mathbf{u}_h^{*,n+\frac{1}{2}}$  at the interfaces of the density control volumes surrounding each node of the triangulation. These interfaces correspond to the dotted lines of the dual mesh  $\tau_h^*$  displayed in Figure 1. Following the same strategy as in the incompressible case [4], this value has to be piecewise constant on each triangle  $K$  of the mesh  $\tau_h$ . In the low-Mach case, it is given by:

$$\mathbf{u}_h^{*,n+\frac{1}{2}}|_K = \frac{3\mathbf{u}_h^{*,n}|_K - \mathbf{u}_h^{*,n-1}|_K}{2}, \quad (21)$$

with:

$$\mathbf{u}_h^{*,n}|_K = \frac{1}{|K|} \int_K \tilde{\mathbf{u}}_h^n - \frac{2 \Delta t}{3 \gamma \bar{\rho}_h^n|_K} \nabla \phi_h^n|_K.$$

**Remark 3.4.** *Definition (21) of  $\mathbf{u}_h^{*,n+\frac{1}{2}}|_K$  allows to ensure that in the case of a constant flow density in space (and consequently also constant in temperature), the scheme preserves the constant states imposed in the continuous model by the incompressibility*

constraint. In other words, the weak divergence property in the sense of the Finite Element projection method (see Remark 3.3) is transferred to the Finite Volume method, as it was proved in the context of a direct resolution by an Uzawa solver in [4].

**Remark 3.5.** In the incompressible case, let us note that the developed scheme allows to preserve the constant states. Indeed, let assume the following properties:

$$\begin{aligned} (H1) \quad P^n &= P^{n-1} = P^{n-2}, & (H3) \quad \rho_h^n &\text{ is constant in space,} \\ (H2) \quad T_h^n &= T_h^{n-1} \text{ are constant in space,} & (H4) \quad \int_{\partial\Omega} \mathbf{u}_D^{n+1} \cdot \mathbf{n} &= 0. \end{aligned}$$

We want to prove that  $T_h^{n+1} = T_h^n$  and  $\rho_h^{n+1} = \rho_h^n$ . First, (17) with assumptions (H1), (H2) and (H4) lead to  $P^{n+1} = P^n$ . Then, the weak formulation of (19) at time  $t^n$  writes:

$$\int_{\Omega_A} \frac{1}{\bar{\rho}_h^n} \nabla \phi_h^n \cdot \nabla \psi_A = \frac{3\gamma}{2\Delta t} \left( \int_{\Omega_A} \nabla \cdot \tilde{\mathbf{u}}_h^n \psi_A + \frac{3P^n - 4P^{n-1} + P^{n-2}}{2\gamma \Delta t P^n} \int_{\Omega_A} \psi_A + \frac{\gamma - 1}{Re Pr P^n} \int_{\Omega_A} \nabla T_h^n \cdot \nabla \psi_A \right),$$

where  $\psi_A$  is the  $\mathbb{P}_1$  basis function associated to an internal node  $A$  and  $\Omega_A$  is the support of  $\psi_A$  (see Figure 1). Assumptions (H1), (H2) and (H4) lead to:

$$\int_{\Omega_A} \left( \tilde{\mathbf{u}}_h^n - \frac{2\Delta t}{3\gamma \bar{\rho}_h^{n+1}} \nabla \phi_h^n \right) \cdot \nabla \psi_A = 0,$$

and definition (20) of  $\mathbf{u}_h^n$  gives:

$$\int_{\Omega_A} \mathbf{u}_h^n \cdot \nabla \psi_A = 0.$$

It is the analogous of relation (23) in [4], which allows to obtain:

$$\int_{\partial C_A} u_h^{*,n} \cdot \mathbf{n} = 0,$$

where  $C_A$  is the FV control volume associated to node  $A$ . Then, (H3) leads to  $\rho_h^{n+1} = \rho_h^n$ . Finally, equation (18) and assumptions (H1) and (H2) give  $T_h^{n+1} = T_h^n$ .

## 4 Numerical simulations

### 4.1 Analytical Benchmarks

#### 4.1.1 Constant density

We first want to illustrate the fact that for incompressible flows, if the density and the temperature are initially homogeneous, then they remain constant (see Remark 3.5).

It was already done for the density in the case of the variable density incompressible system using an Uzawa solver (see [4]). To do this, we consider the following analytical solution:

$$\left\{ \begin{array}{l} \mathbf{u}_{\text{ex}}(x, y) = 4 \left( \frac{-y(x-1)^2(x+1)^2(y-1)(y+1)}{x(y-1)^2(y+1)^2(x-1)(x+1)} \right), \\ \rho_{\text{ex}} = 1, \\ T_{\text{ex}} = \frac{1}{\gamma - 1} \\ P_{\text{ex}} = 1, \\ \pi_{\text{ex}} = 0, \end{array} \right. \quad (22)$$

in the square domain  $\Omega = [-1, 1]^2$ . A source term in the right hand side of equation (2) is consequently added instead of the gravity term. Boundary conditions are Dirichlet ones on the whole boundary of  $\Omega$  for all variables (i.e.  $\Gamma_D = \partial\Omega$ ). Simulations are performed on unstructured meshes at  $\text{Re} = 1$  and  $\text{Pr} = \gamma$  up to time  $t_f = 1 = N\Delta t$  with  $\Delta t = h_{max} = 0.0625$  and  $h_{max}$  the maximum space step of the mesh. We give in Table 1 the values of  $\max_{0 \leq n \leq N} \|\rho_h^n - \rho_{\text{ex}}\|_{L^\infty(\Omega)}$  and  $\max_{0 \leq n \leq N} \|T_h^n - T_{\text{ex}}\|_{L^\infty(\Omega)}$ .

$\max_{0 \leq n \leq N} \ \rho_h^n - \rho_{\text{ex}}\ _{L^\infty(\Omega)}$	$\max_{0 \leq n \leq N} \ T_h^n - T_{\text{ex}}\ _{L^\infty(\Omega)}$
2.56e-13	1.09e-13

Table 1: Constant density case, errors in density and temperature.

We observe on Table 1 that the density and the temperature remain constant nearly to the machine error during the whole simulation time, as it can be seen at the final time  $t_f$  in Figure 2 on the mesh corresponding to  $h_{max} = 0.0625$ . We observe that the density local maximum error is located in the vicinity of the boundaries. This well-balanced property of the scheme ensures the preservation of the constant values of density and temperature, in the case where the velocity field is divergence free.

#### 4.1.2 Analytical solution

Now, in order to investigate the accuracy of the scheme, convergence tests are performed for a non-solenoidal velocity field. The analytical solution is given by:

$$\left\{ \begin{array}{l} \mathbf{u}_{\text{ex}}(t, x, y) = -\frac{1}{\gamma(2 + \sin(2\pi t))} \left( \frac{2(\gamma - 1)(2 + \cos(2\pi t))}{(1 + x^2 + y^2)^2} + \pi \cos(2\pi t) \right) \begin{pmatrix} x \\ y \end{pmatrix}, \\ \rho_{\text{ex}}(t, x, y) = \frac{2 + \sin(2\pi t)}{(\gamma - 1)(2 + \cos(2\pi t))} (1 + x^2 + y^2), \\ T_{\text{ex}}(t, x, y) = \frac{2 + \cos(2\pi t)}{1 + x^2 + y^2}, \\ P_{\text{ex}}(t) = 2 + \sin(2\pi t), \\ \pi_{\text{ex}}(t, x, y) = \sin(x) \sin(y) \sin(2\pi t), \end{array} \right. \quad (23)$$

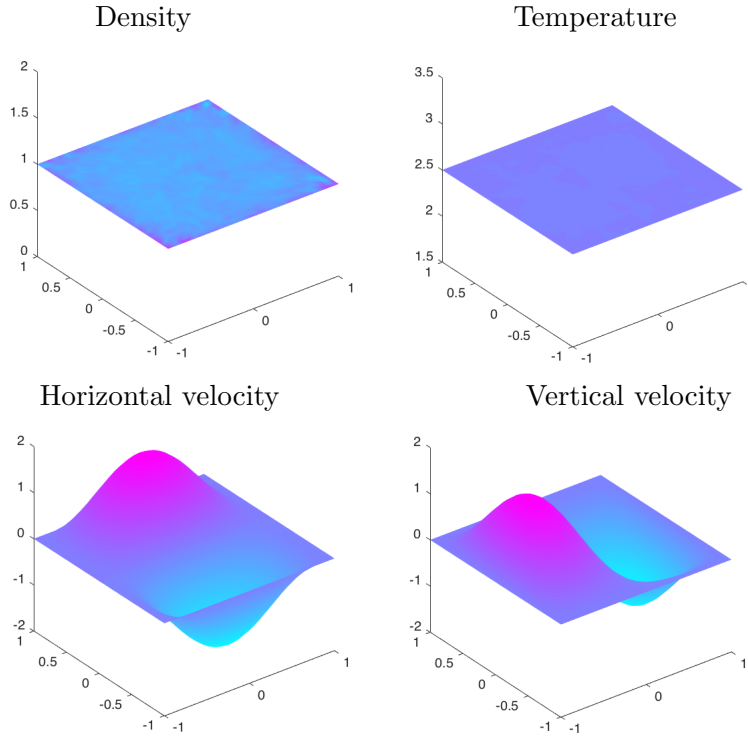


Figure 2: Density, temperature and the two velocity components at  $t_f = 1$ , for the mesh  $h_{max} = 0.0625$ .

in the square  $\Omega = [-1, 1]^2$ . The Reynolds and Prandtl numbers are respectively equal to 1 and  $\gamma$ , the gravity term is not considered and appropriated source terms are added in the right-hand-sides of equations (1), (2) and (3). Dirichlet boundary conditions are considered on the whole boundary of  $\Omega$  for the velocity, and non-homogeneous Neumann boundary conditions are prescribed on the whole boundary of  $\Omega$  for the temperature and density (i.e.  $\Gamma_N = \partial\Omega$ ).

The simulations are performed on unstructured grids in the range  $1/150 \leq h_{max} \leq 1/50$ , up to the final time  $t_f = 0.2$ , using  $\Delta t = h_{max}$ . In order to evaluate the performances of the splitting proposed in section 3.1, the C-FV-FE scheme results are compared with the ones obtained using some fixed-point iterations, following the same idea as in [2] (see Appendix A for the description of the corresponding fixed-point algorithm). In that case, the fixed-point iterations are performed until the  $L^2$ -norm of two successive iterates is smaller than  $10^{-10}$  for all variables. From the practical point of view, we observe that the fixed point converges in 6 or 7 iterations for the worst cases. Finally, these results are also compared to those obtained with one of the schemes proposed in [2] (pressure-based solver, asymptotic approach 1), for which some fixed-point iterations are required.

We observe, whatever the considered scheme, that the thermodynamic pressure  $P$  converges at order 2 in the  $L^\infty(0, t_f)$  norm. We plot in Figure 3 the  $L^\infty(0, t_f; L^2(\Omega))$

norm of the errors on the density  $\rho_h$ , the temperature  $T_h$ , the velocity  $\mathbf{u}_h$  and the dynamic pressure  $\pi_h$  as a function of  $h_{max}$  in a log/log scale. On one hand, all schemes provide a convergence rate at order 2 for the density, the temperature and the velocity. Concerning the dynamic pressure, a rate slightly larger than 1.5 is obtained. More precisely, for the C-FV-FE scheme, a rate between 1.65 and 1.85 is observed, as we can see in Table 2. These results are in good agreement with the incompressible constant density case, for which it was proved in [17] that the errors in time in the  $L^2(\Omega)$ -norm for the velocity and the pressure are of order 2 and  $3/2$  respectively. In fact, the numerical convergence rate obtained for the dynamic pressure is slightly better than the theoretical expected one. On the other hand, we can see that the results obtained using the C-FV-FE scheme with or without a fixed-point iterations procedure correspond to the same orders of convergence. In particular, the errors are quite the same, except a small difference in the density error. In conclusion, the fixed-point iterations are not necessary for the C-FV-FE scheme. Furthermore, it should be pointed out that the fixed-point iterations are crucial for the scheme proposed in [2]. Indeed, without the fixed-point iterations, the scheme does not converge for the dynamic pressure, and orders of convergence are smaller than one for the velocity and the temperature.

In Figure 4, we plot the  $L^\infty(0, t_f; L^2(\Omega))$  error on the discrete state equation, defined by:

$$err_h = \max_{0 \leq n \leq N} \left\| T_h^n - \frac{P^n}{(\gamma - 1)\rho_h^n} \right\|_{L^2(\Omega)},$$

obtained with the C-FV-FE scheme. As explained in section 2.1, the state equation is imposed implicitly. As we can see,  $err_h$  converges towards zero at order 2, what corresponds to the expected behaviour because of the previous convergence rates obtained in  $\rho_h$ ,  $T_h$  and  $P$ .

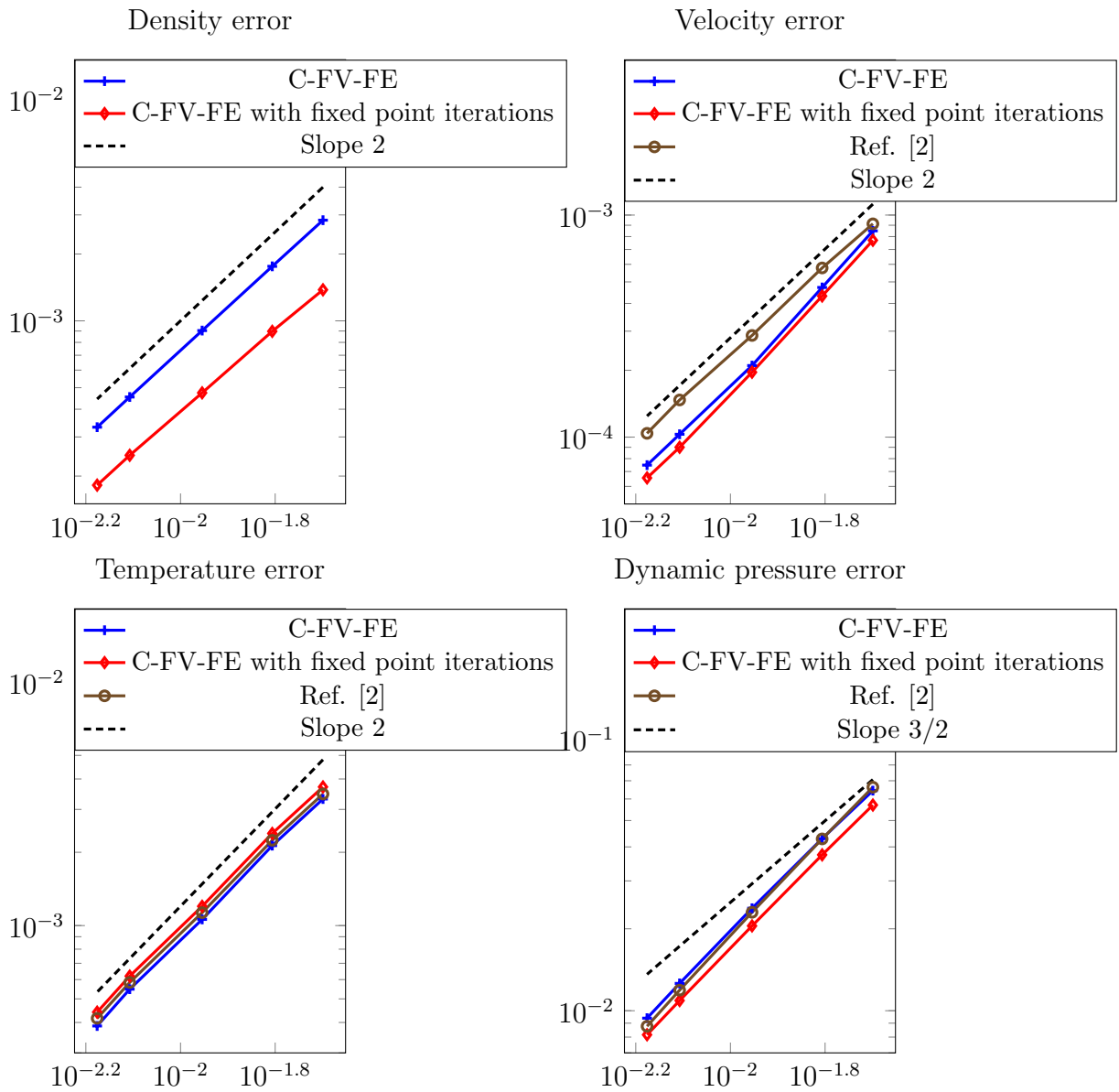


Figure 3: Errors in  $L^\infty(0, t_f; L^2(\Omega))$  norm versus  $h_{max}$ , log/log scale.

$h_{max}$	Error $P$	Rate	Error $\rho$	Rate	Error $T$	Rate	Error $u$	Rate	Error $\pi$	Rate
2.00e-2	5.12e-3	-	2.84e-3	-	3.31e-3	-	8.49e-4	-	6.44e-2	-
1.56e-2	3.31e-3	1.76	1.76e-3	1.94	2.13e-3	1.79	4.72e-4	2.38	4.29e-2	1.65
1.11e-2	1.74e-3	1.89	9.04e-4	1.95	1.06e-3	2.05	2.10e-4	2.38	2.38e-2	1.73
7.81e-3	8.95e-4	1.89	4.54e-4	1.96	5.48e-4	1.87	1.03e-4	2.02	1.26e-2	1.80
6.67e-3	6.53e-4	1.99	3.32e-4	1.97	3.87e-4	2.19	7.48e-5	2.02	9.39e-3	1.85

Table 2: C-FV-FE scheme. Errors in  $L^\infty(0, t_f; L^2(\Omega))$  norm and corresponding convergence rates.

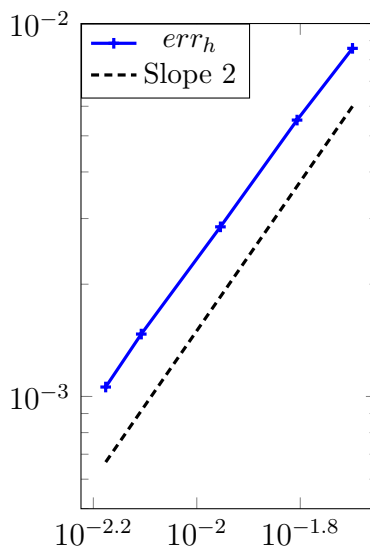


Figure 4: Error in  $L^\infty(0, t_f; L^2(\Omega))$  norm on the discrete state equation versus  $h_{max}$ , C-FV-FE scheme, log/log scale.

## 4.2 The transient injection flow

This benchmark was initially proposed in [2] and also considered in [11] and [1]. Considering the adimensioned equations, the domain is defined by a rectangle  $\Omega = [-1.5; 1.5] \times [0; 7]$  (see Figure 5), defining a cavity in which a calorifically perfect gas is initially at rest. The initial temperature and thermodynamic pressure values are given by:

$$T_0 = 300 \quad \text{and} \quad P_0 = 1. \quad (24)$$

The Reynolds, the Prandtl and the Froude numbers of the fluid are respectively equal to  $Re = 40$ ,  $Pr = 0.71$  and  $Fr = 0.042$ . Zero Dirichlet boundary conditions for the velocity and zero Neumann ones for the temperature are specified on all boundaries, except for a small hole in the bottom wall defined by  $\Gamma_D = \left[-\frac{l}{2}; \frac{l}{2}\right] \times \{0\}$ , with  $l = 0.2$ :

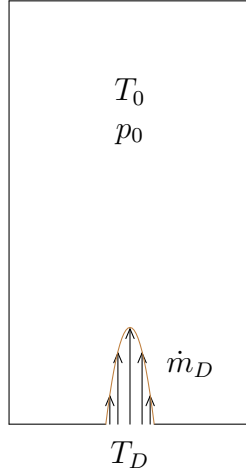


Figure 5: The cavity  $\Omega$ .

$$\begin{aligned} \mathbf{u}(t, x, y)|_{\partial\Omega \setminus \Gamma_D} &= \mathbf{0}, \\ \nabla T \cdot \mathbf{n}|_{\partial\Omega \setminus \Gamma_D} &= 0. \end{aligned}$$

On  $\Gamma_D$ , the fluid is injected at the temperature  $T_D = 600$ , subject to a parabolic inflow profile. The momentum is imposed from  $t = 0$  up to  $t_f = 6$  by:

$$(\rho \mathbf{u})_D(x, y) = \left( 0 ; \frac{6 \times 2.87 \cdot 10^{-3} \dot{m}_D}{l^2 (\gamma - 1)} \left( \frac{l^2}{4} - x^2 \right) \right)^T \text{ for } 0 \leq t \leq 6, \quad (25)$$

where  $\dot{m}_D = 1$  is the average momentum. Because of this kind of boundary condition, the C-FV-FE scheme has to be a little adapted. As in [2], instead of solving (10), we first compute the new pressure  $P^{n+1}$  by solving a global conservation of mass equation associated to an extrapolation of the temperature, namely:

$$P^{n+1} = ((\gamma - 1)|\Omega|\rho_0 + 2.87 \cdot 10^{-3} \dot{m}_D l t^{n+1}) \left( \int_{\Omega} \frac{1}{2T^n - T^{n-1}} \right)^{-1}. \quad (26)$$

Then, the velocity is updated on  $\Gamma_D$ :

$$\mathbf{u}_D^{n+1} = \left( 0, \frac{2.87 \cdot 10^{-3} T_D 6 \dot{m}_D}{P^{n+1} l^2} \left( \frac{l^2}{4} - x^2 \right) \right)^T = \left( 0, \frac{258.3}{P^{n+1}} \left( \frac{l^2}{4} - x^2 \right) \right)^T,$$

and the following of the scheme remains the same.

Note that in [11] and [1], different boundary conditions are considered. Consequently, the time evolution of the temperature is relatively similar but not exactly comparable with the results presented in [2]. If the boundary conditions given in [11]

are enforced in the C-FV-FE scheme, we can observe analogous temperature distribution and velocity field as those presented in [11].

First of all, we check the grid convergence property. We use some structured meshes like the one displayed in Figure 6. We plot in Figure 7 the isovalues of the temperature at  $t_f = 6$ . Results are obtained on three meshes corresponding respectively to grids  $60 \times 60$ ,  $120 \times 120$  and  $180 \times 180$ , and using  $\Delta t = h_{max}$ . Even if the jet obtained with the  $60 \times 60$  grid seems to be a little delayed, we can see by comparing the solutions obtained for grids  $120 \times 120$  and  $180 \times 180$  that they are very close to each other. Also, we plot in Figure 8 the evolution of the velocity components  $u_x$  and  $u_y$  and of the temperature  $T$  along the vertical lines  $x = 0$ ,  $x = -L/4$  and horizontal ones  $y = H/4$ ,  $y = H/2$  and  $y = 3H/4$  at  $t = 6$ . The temperature distribution and the velocity field are nearly the same in both cases, so that the grid convergence can be considered as achieved.

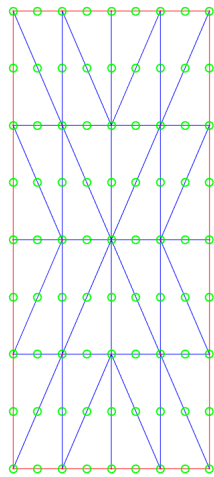


Figure 6: Grid Mesh  $4 \times 4$ .

In order to confirm the observations made in section 4.1.2, we compare in Figure 9 the velocity and temperature distributions obtained with the C-FV-FE scheme and with the scheme from [2] (pressure-based solver, asymptotic approach 1 with 15 iterations in the fixed-point process) at time  $t_f = 6$  on a  $120 \times 120$  grid. These solutions look very similar and are in good agreement with those reported in [2]. Nevertheless, although the shape of the cross-sections showed in Figure 8 are comparable to the profiles plotted in Figures 8 and 9 in [2], the amplitudes obtained with the C-FV-FE scheme are slightly greater than those computed in [2]. These differences can be explained by the ability of our scheme to preserve locally the density of the fluid.

Finally, we want to investigate the thermodynamic pressure evolution. Similarly to [2], neglecting the diffusive term in (9), we get:

$$\frac{dP}{dt} + \frac{\gamma P}{|\Omega|} \int_{\Gamma_D} \mathbf{u} \cdot \mathbf{n} \simeq 0. \quad (27)$$

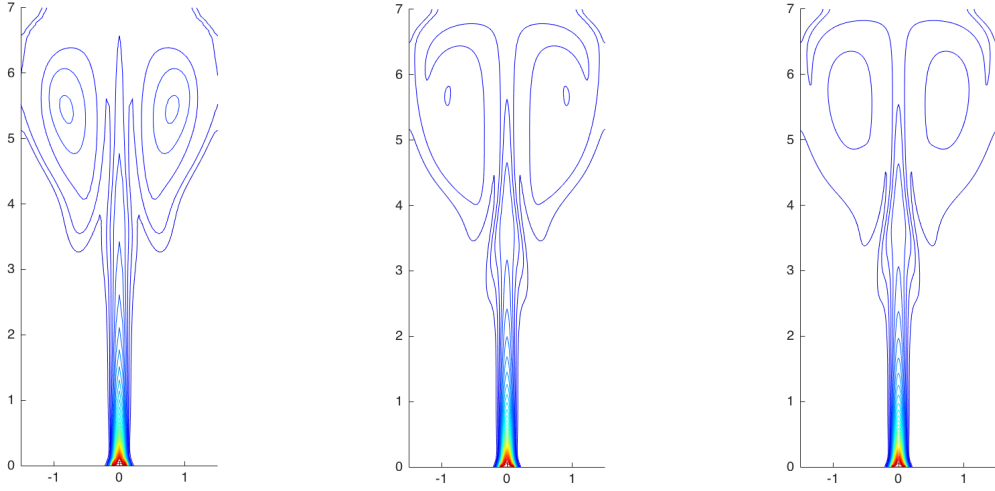


Figure 7: C-FV-FE scheme, temperature at  $t = 6$ . From the left to the right: Grids  $60 \times 60$ ,  $120 \times 120$  and  $180 \times 180$ . 40 isovalues from 330 to 600, uniform distribution.

Using the value of  $(\rho \mathbf{u})_D$  given in (25), and the state equation (4) to evaluate  $\rho_D$ , we can explicitly solve (27) to obtain an approximation of the thermodynamic pressure:

$$P(t) \simeq P_0 + \frac{258.3 \gamma}{750 |\Omega|} t. \quad (28)$$

Figure 10 displays the evolution of the approximate thermodynamic pressure given by (28), the one computed with the C-FV-FE scheme by equation (26) and also by the scheme from [2] on a  $120 \times 120$  grid. Once again, results are close to each other.

**Remark 4.1.** *In order to give a justification to the approximation used in the derivation of (27), we computed the average values in time of  $\frac{\gamma P}{|\Omega|} \int_{\partial\Omega} \mathbf{u} \cdot \mathbf{n}$  and  $\frac{\gamma(\gamma - 1)}{|\Omega| Re Pr} \int_{\partial\Omega} \nabla T \cdot \mathbf{n}$  with the C-FV-FE scheme, and obtained the values of  $2.26e - 02$  and  $4.62e - 04$  respectively. Consequently, as the second term is two orders of magnitude below the first one, here it can be neglected. This fact can also explain that the pressure given by (28) is slightly lower than the one computed using the C-FV-FE scheme, since the second term is not only very small, but also positive.*

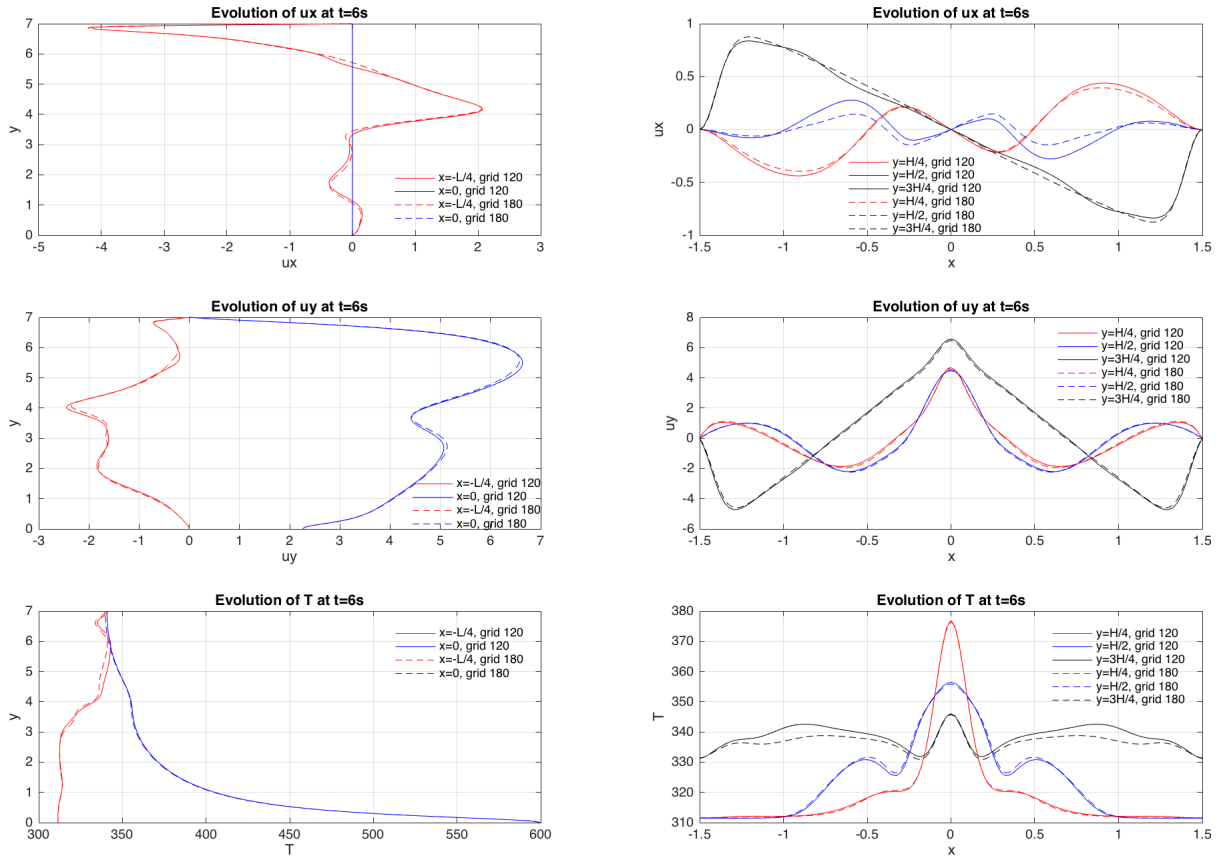


Figure 8: Evolution of  $u_x$ ,  $u_y$  and  $T$  along the lines  $x = 0$ ,  $x = -L/4$ ,  $y = H/4$ ,  $y = H/2$  and  $y = 3H/4$  at  $t = 6$ , for the grids  $120 \times 120$  and  $180 \times 180$ .

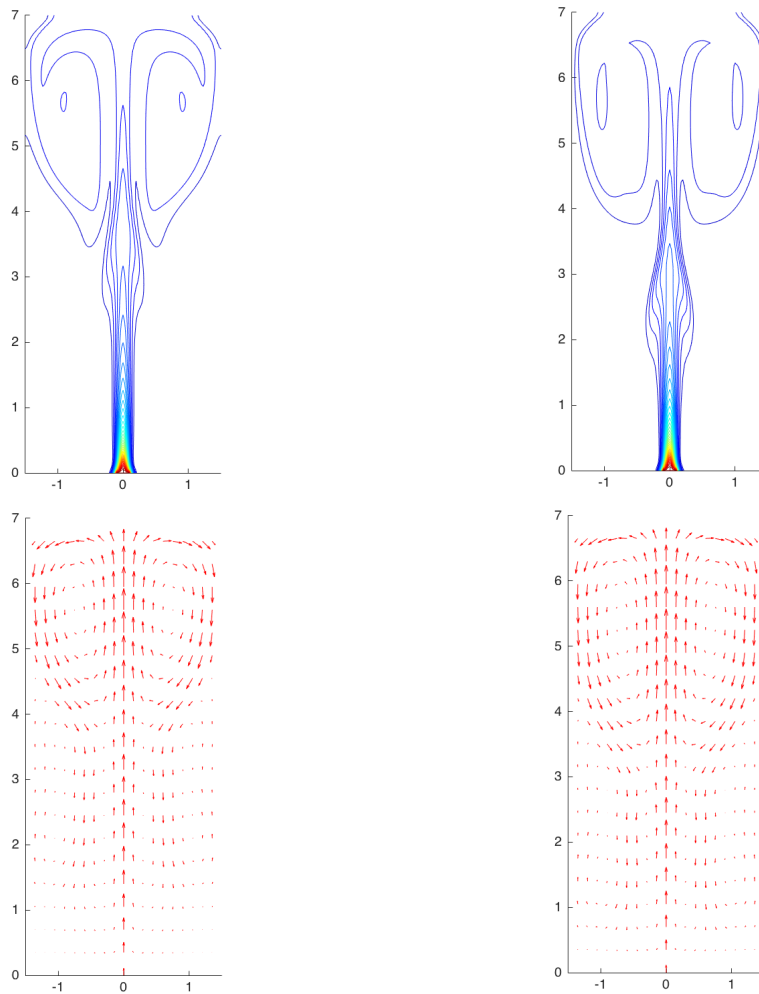


Figure 9: Temperature and velocity at  $t = 6$ . Left: C-FV-FE scheme. Right: scheme in Ref. [2]. Top: temperature - 40 isovalues from 330 to 600, uniform distribution. Bottom: velocity.

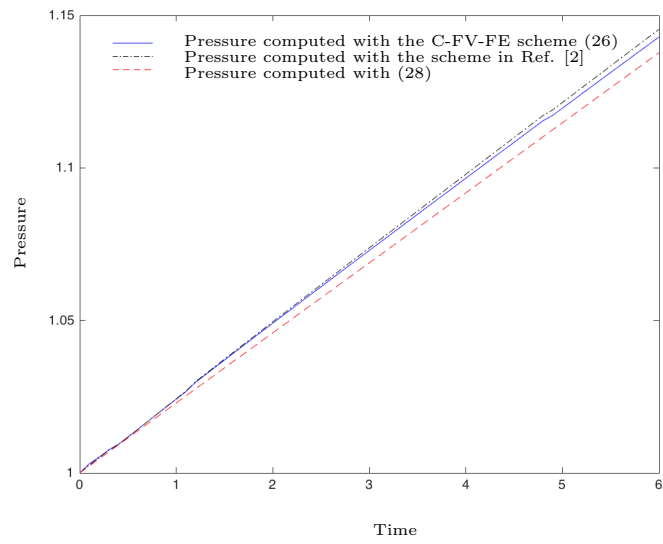


Figure 10: Evolution of the thermodynamic pressure.

## 5 Conclusion

In this article, a combined Finite Volume - Finite Element method based on a time splitting has been developed. The main ingredients are:

- to solve the mass conservation equation by a FV method instead of exploiting the equation of state;
- to solve the temperature and the momentum equations by a FE method, using a projection method in order to fulfill the constraint (5);
- to keep a particular definition of the velocity (see (21)) in order to verify the divergence constraint also in the FV scheme.

We have compared the numerical results of our C-FV-FE method with those obtained implementing one of the schemes proposed in [2], showing that all of them are of order two. We have also verified that our scheme allows to preserve the constant states as well as the maximum principle on the density at the incompressible limit of the fluid. We underline that a fixed-point iterations procedure is not necessary, and consequently the C-FV-FE scheme achieves the computation faster than other schemes proposed in the literature. Finally, we have investigated a problem of injection of hot gas into a cavity filled with the same gas, obtaining results very similar to those reported in the literature. Nevertheless, the adequacy of the C-FV-FE method for more challenging laminar or turbulent flow situations remains to be investigated. We intend to do this in a future work.

## Acknowledgements

This work was supported in part by the Labex CEMPI (ANR-11-LABX-0007-01).

## A Appendix

In this section, we will detail the fixed-point iterations algorithm. We perform a loop of index  $l$ . Knowing  $P^{n+1,l}$ ,  $T^{n+1,l}$ ,  $\mathbf{u}^{n+1,l}$  and  $\pi^{n+1,l}$ , we show how to compute  $P^{n+1,l+1}$ ,  $T^{n+1,l+1}$ ,  $\mathbf{u}^{n+1,l+1}$  and  $\pi^{n+1,l+1}$ . Note that for a generic variable  $a$ ,  $a^{n+1,0} = a^n$ .

1. The new density  $\rho^{n+1,l+1}$  is computed by solving:

$$\frac{\rho^{n+\frac{1}{2},l+1} - \rho^n}{\Delta t} + \nabla \cdot (\rho^n \mathbf{u}^{n+\frac{1}{2},l}) = 0, \quad (29)$$

$$\frac{\rho^{n+1,l+1} - \rho^n}{\Delta t} + \frac{1}{2} \left( \nabla \cdot (\rho^n \mathbf{u}^{n+\frac{1}{2},l}) + \nabla \cdot (\rho^{n+\frac{1}{2},l+1} \mathbf{u}^{n+\frac{1}{2},l}) \right) = 0, \quad (30)$$

with:

$$\mathbf{u}^{n+\frac{1}{2},l} = \frac{\mathbf{u}^n + \mathbf{u}^{n+1,l}}{2}.$$

2. The thermodynamic pressure  $P^{n+1,l+1}$  is computed by:

$$\frac{3P^{n+1,l+1} - 4P^n + P^{n-1}}{2\Delta t} + \frac{\gamma P^{n+1,l+1}}{|\Omega|} \int_{\partial\Omega} \mathbf{u}_D^{n+1} \cdot \mathbf{n} = \frac{\gamma(\gamma-1)}{|\Omega|\text{Re Pr}} \int_{\Gamma_D} \nabla T^{n+1,l} \cdot \mathbf{n}. \quad (31)$$

3. The temperature  $T^{n+1,l+1}$  is computed by solving:

$$\begin{aligned} & \rho^{n+1,l+1} \left( \frac{3T^{n+1,l+1} - 4T^n + T^{n-1}}{2\Delta t} + \mathbf{u}^{n+1,l} \cdot \nabla T^{n+1,l} \right) \\ & - \frac{1}{\gamma} \left( \frac{3P^{n+1,l+1} - 4P^n + P^{n-1}}{2\Delta t} \right) - \frac{1}{\text{Re Pr}} \Delta T^{n+1,l+1} = 0, \end{aligned} \quad (32)$$

4. The velocity  $\mathbf{u}^{n+1,l+1}$  and the pressure  $\pi^{n+1,l+1}$  are computed by solving:

$$\begin{aligned} & \rho^{n+1,l+1} \left( \frac{3\mathbf{u}^{n+1,l+1} - 4\mathbf{u}^n + \mathbf{u}^{n-1}}{2\Delta t} + \mathbf{u}^{n+1,l} \cdot \nabla \mathbf{u}^{n+1,l} \right) + \frac{1}{\gamma} \nabla \pi^{n+1,l+1} \\ & - \frac{1}{\text{Re}} \nabla \cdot \boldsymbol{\tau}^{n+1,l+1} = -\frac{1}{\text{Fr}^2} \rho^{n+1,l+1} \mathbf{e}_y, \\ \nabla \cdot \mathbf{u}^{n+1,l+1} & = -\frac{3P^{n+1,l+1} - 4P^n + P^{n-1}}{2\gamma\Delta t P^{n+1,l+1}} + \frac{\gamma-1}{\text{Re Pr} P^{n+1,l+1}} \Delta T^{n+1,l+1}, \end{aligned}$$

with

$$\nabla \cdot \boldsymbol{\tau}^{n+1,l+1} = \Delta \mathbf{u}^{n+1,l+1} + \frac{1}{3} \nabla (\nabla \cdot \mathbf{u}^{n+1,l}).$$

## References

- [1] M. Avila, J. Principe, and R. Codina. A finite element dynamical nonlinear sub-scale approximation for the low Mach number flow equations. *J. Comput. Phys.*, 230(22):7988–8009, 2011.
- [2] A. Beccantini, E. Studer, S. Gounand, J.-P. Magnaud, T. Kloczko, C. Corre, and S. Kudriakov. Numerical simulations of a transient injection flow at low Mach number regime. *Internat. J. Numer. Methods Engrg.*, 76(5):662–696, 2008.
- [3] C. Calgario, E. Chane-Kane, E. Creusé, and T. Goudon.  $L^\infty$ -stability of vertex-based MUSCL finite volume schemes on unstructured grids: simulation of incompressible flows with high density ratios. *J. Comput. Phys.*, 229(17):6027–6046, 2010.
- [4] C. Calgario, E. Creusé, and T. Goudon. An hybrid finite volume-finite element method for variable density incompressible flows. *J. Comput. Phys.*, 227(9):4671–4696, 2008.

- [5] C. Calgario, E. Creusé, and T. Goudon. Modeling and simulation of mixture flows: application to powder-snow avalanches. *Comput. & Fluids*, 107:100–122, 2015.
- [6] A. J. Chorin. Numerical solution of the Navier-Stokes equations. *Math. Comp.*, 22:745–762, 1968.
- [7] A. J. Chorin. On the convergence of discrete approximations to the Navier-Stokes equations. *Math. Comp.*, 23:341–353, 1969.
- [8] P. G. Ciarlet. *The finite element method for elliptic problems*. North-Holland Publishing Co., Amsterdam-New York-Oxford, 1978. Studies in Mathematics and its Applications, Vol. 4.
- [9] S. Dellacherie. On a diphasic low Mach number system. *M2AN Math. Model. Numer. Anal.*, 39(3):487–514, 2005.
- [10] V. Gravemeier and W. A. Wall. An algebraic variational multiscale-multigrid method for large-eddy simulation of turbulent variable-density flow at low Mach number. *J. Comput. Phys.*, 229(17):6047–6070, 2010.
- [11] V. Gravemeier and W. A. Wall. Residual-based variational multiscale methods for laminar, transitional and turbulent variable-density flow at low Mach number. *Internat. J. Numer. Methods Fluids*, 65(10):1260–1278, 2011.
- [12] J. L. Guermond, P. Mineev, and J. Shen. An overview of projection methods for incompressible flows. *Comput. Methods Appl. Mech. Engrg.*, 195(44-47):6011–6045, 2006.
- [13] J.-L. Guermond and L. Quartapelle. Calculation of incompressible viscous flows by an unconditionally stable projection FEM. *J. Comput. Phys.*, 132(1):12–33, 1997.
- [14] J.-L. Guermond and L. Quartapelle. On stability and convergence of projection methods based on pressure Poisson equation. *Internat. J. Numer. Methods Fluids*, 26(9):1039–1053, 1998.
- [15] J.-L. Guermond and A. Salgado. A splitting method for incompressible flows with variable density based on a pressure Poisson equation. *J. Comput. Phys.*, 228(8):2834–2846, 2009.
- [16] J.-L. Guermond and A. J. Salgado. Error analysis of a fractional time-stepping technique for incompressible flows with variable density. *SIAM J. Numer. Anal.*, 49(3):917–944, 2011.
- [17] J. L. Guermond and J. Shen. On the error estimates for the rotational pressure-correction projection methods. *Math. Comp.*, 73(248):1719–1737 (electronic), 2004.

- [18] H. Guillard and C. Viozat. On the behaviour of upwind schemes in the low Mach number limit. *Comput. & Fluids*, 28(1):63–86, 1999.
- [19] V. Heuveline. On higher-order mixed FEM for low Mach number flows: application to a natural convection benchmark problem. *Internat. J. Numer. Methods Fluids*, 41(12):1339–1356, 2003.
- [20] B. Lessani and M. V. Papalexandris. Time-accurate calculation of variable density flows with strong temperature gradients and combustion. *J. Comput. Phys.*, 212(1):218–246, 2006.
- [21] P.-L. Lions. *Mathematical topics in fluid mechanics. Vol. 2*, volume 10 of *Oxford Lecture Series in Mathematics and its Applications*. The Clarendon Press, Oxford University Press, New York, 1998. Compressible models, Oxford Science Publications.
- [22] W. Liu and G. Makhviladze. An implicit finite element solution of thermal flows at low Mach number. *J. Comput. Phys.*, 227(5):2743–2757, 2008.
- [23] H. Luo, Baum J.D., and R. Lohner. Extension of harten-lax-van leer scheme for flows at all speeds. *AIAA Journal*, 43(6):1160–1166, 2005.
- [24] A. Majda and J. Sethian. The derivation and numerical solution of the equations for zero Mach number combustion. *Combustion Science and Technology*, 42:185–205, 1985.
- [25] M. J. Martinez and D. K. Gartling. A finite element method for low-speed compressible flows. *Comput. Methods Appl. Mech. Engrg.*, 193(21-22):1959–1979, 2004.
- [26] C.-D. Munz, S. Roller, R. Klein, and K. J. Geratz. The extension of incompressible flow solvers to the weakly compressible regime. *Comput. & Fluids*, 32(2):173–196, 2003.
- [27] F. Nicoud. Conservative high-order finite-difference schemes for low-Mach number flows. *J. Comput. Phys.*, 158(1):71–97, 2000.
- [28] S. Noelle, G. Bispen, K. R. Arun, M. Lukáčová-Medvidová, and C.-D. Munz. A weakly asymptotic preserving low Mach number scheme for the Euler equations of gas dynamics. *SIAM J. Sci. Comput.*, 36(6):B989–B1024, 2014.
- [29] J. Principe and R. Codina. A stabilized finite element approximation of low speed thermally coupled flows. *International Journal of Numerical Methods for Heat and Fluid Flow*, 18:835–867, 2007.
- [30] J. Principe and R. Codina. Mathematical models for thermally coupled low speed flows. *Advances in Theoretical and Applied Mechanics 2*, pages 93–112, 2009.

- [31] R. Temam. *Navier-Stokes equations. Theory and numerical analysis*. North-Holland Publishing Co., Amsterdam-New York-Oxford, 1977. Studies in Mathematics and its Applications, Vol. 2.
- [32] E. Turkel. Preconditioned methods for solving the incompressible and low speed compressible equations. *Journal of Computational Physics*, 72:277–298, 1987.